Imaging tripartite synapses using super-resolution microscopy

Janosch Peter Heller[a,b,]*, Tuamoru Odii[a,c], Kaiyu Zheng[a], Dmitri A. Rusakov[a,]*

[a] *UCL Queen Square Institute of Neurology, University College London, London, United Kingdom*
[b] *FutureNeuro Research Centre, Royal College of Surgeons in Ireland, Dublin, Ireland*
[c] *Department of Physiology, Faculty of Basic Medical Sciences, Alex Ekwueme Federal University Ndufu-Alike Ikwo, PMB 1010 Abakaliki, Nigeria*

ABSTRACT

Astroglia are vital facilitators of brain development, homeostasis, and metabolic support. In addition, they are also essential to the formation and regulation of synaptic circuits. Due to the extraordinary complex, nanoscopic morphology of astrocytes, the underlying cellular mechanisms have been poorly understood. In particular, fine astrocytic processes that can be found in the vicinity of synapses have been difficult to study using traditional imaging techniques.

Here, we describe a 3D three-colour super-resolution microscopy approach to unravel the nanostructure of tripartite synapses. The method is based on the SMLM technique direct stochastic optical reconstruction microscopy (dSTORM) which uses conventional fluorophore-labelled antibodies. This approach enables reconstructing the nanoscale localisation of individual astrocytic glutamate transporter (GLT-1) molecules surrounding presynaptic (bassoon) and postsynaptic (Homer1) protein localisations in fixed mouse brain sections. However, the technique is readily adaptable to other types of targets and tissues.

1. Introduction

1.1. The nanoscopic nature of astrocytes and their involvement in synaptic transmission

Over the last decade, neuroglia, formerly considered a mere neuron-supportive cell group, have emerged as active partners of neurons in information acquisition, processing, integration and storage [reviewed in 1–3]. Astrocytes and astrocyte-like cells can be found throughout the nervous system. Protoplasmic astrocytes reside in the grey matter where they occupy non-overlapping territories [4–6]. These cells derive their name from their star-like appearance as they extend several primary processes from the soma, which in turn give off secondary branches. From these, a myriad of delicate, nanoscopic protrusions emanate which confer a sponge-like appearance to the cells [reviewed in 7,8]. This complex morphology makes direct physiological probing of astrocytes inherently problematic. The soma and stem processes make up the astrocyte's microstructure visible under diffraction-limited optical microscopes. However, they only constitute 15% of the astrocytic cellular volume and about 20% of the cell's surface area [4]. The bulk of an astrocyte is thus made up by the nanoscopic protrusions which mediate key astrocytic functions. In addition to their involvement in neuronal signal transduction, astrocytes play essential roles in brain homeostasis [9]. Astrocytes are part of the blood–brain-barrier [10] and operate the lymphatic system [11]. They also regulate local blood flow [12] and provide metabolic support through lactate shuttling [13], and glycogen synthesis and storage [14]. Astroglia are also involved in chemosensing and pH regulation [15], regulate overall energy balance and food intake [15], as well as sleep homeostasis [16]. Furthermore, these cells regulate neurogenesis, neuronal development and guidance [17] as well as synaptogenesis, and synaptic maintenance, elimination and plasticity [18,19]. Astroglia also regulate water, ion and neurotransmitter homeostasis [20–25]. Owing to their critical role in normal brain function and health, astroglia dysfunction can lead to, and is a hallmark of, most if not all neurodegenerative disorders; in the context of pathophysiology, astrocytes are a promising target for therapeutic intervention [26–28].

The capacity of astrocytes to co-ordinate signal transduction in the brain has been associated with their overall size: it is thought that the bigger the astrocyte relative to neurons, the more synapses it can spontaneously or simultaneously co-ordinate and possibly integrate [29–31]. Although neuronal activity remains the *sine qua non* of brain function, it is the capacity or ability of astrocytes to integrate them that might arguably affect the efficiency of brain function, and ultimately the apparent brain capacity [29,32,33].

The main signalling pathways by which astrocytes respond to

* Corresponding authors at: UCL Queen Square Institute of Neurology, University College London, London, United Kingdom.
  E-mail addresses: j.heller@ucl.ac.uk (J.P. Heller), d.rusakov@ucl.ac.uk (D.A. Rusakov).

neuronal activity at synapses are mediated by calcium [reviewed in [34,35,36]. Changes in synaptic activity are picked up by the receptors and transporters on the astrocytic membrane, 'interpreted' in the cytoplasm and often responded to through the release of calcium from intracellular stores leading to further downstream responses, such as release of signalling molecules that modulate neuronal activity [reviewed in [1,37,38].

The emerging realisation that astrocytes are fundamental components of nervous system function has prompted increased research efforts into astrocyte biology. However, due to the complex nanoanatomy of these cells, the molecular underpinnings of astroglia-neuron signalling have not been satisfactorily investigated or fully understood. One key methodological limitation in monitoring live astroglia is that conventional optical microscopes cannot resolve structures beyond the diffraction limit of ~250 nm in the imaging plane and ~600 nm in the z direction [39,40] (see below). Therefore, electron microscopy (EM) has traditionally been used to study synapses as well as nearby astrocytic structures. With the aid of EM, the fine astrocytic processes can be seen projecting towards excitatory synapses [41,42], enwrapping both the pre- and postsynaptic specialisations with a greater affinity for the postsynaptic elements [43–45]. These astrocytic protrusions, often called perisynaptic astrocytic processes (PAPs), show regional and developmental heterogeneity but can be found in close apposition to most excitatory synapses [reviewed in [7,8,46]. Because their diameter could be as small as 50 nm [8,47,48], they have traditionally only been visualised with 3D EM. However, 3D EM methods are costly, time-consuming and resource-demanding to operate. More importantly, even the most accurate immuno-labelling EM studies have not been able to provide a contiguous 3D picture conveying the spatial arrangement of key astroglial proteins and the underlying cellular structures on the nanoscale. Therefore, recent efforts to elucidate functional nano-organisation of astrocytes have concentrated on novel super-resolution microscopy techniques [49–53].

1.2. Breaking the diffraction limit

The physical nature of light as electromagnetic waves imposes a limit on optical resolution: in simple terms, the light source size cannot be smaller than the light half-wavelength or the main part of it. This diffraction limit determines the smallest resolvable distance, generally in accord with Ernst Abbe's equation $d = 0.5\lambda/NA$ (where λ is wavelength, and NA is the objective's numerical aperture), which in the case of conventional optical microscopes is normally 200 nm or higher. Thus, any point (infinitesimally small) source of light in a specimen will be represented as a 3D point spread function (PSF) characteristic of an optical system. The PSF thus provides a standard measure of resolution. Its shape determines the full width at half-maximum (FWHM) for a point-source intensity profile, a resolution criterion used extensively in image analysis.

Whilst some insights into fine astroglial morphology can be achieved by diffraction-insensitive imaging techniques employing conventional optics [45,54], the ongoing revolution in microscopy has been providing new optical methods to increase resolution beyond the diffraction limit [reviewed in 39,55,56]. The most widely used applications are structured illumination microscopy (SIM) [57], stimulated emission depletion (STED) microscopy [58] and single molecule localisation microscopy (SMLM) [59]. SIM is based on the concept of spatially varying excitation light intensity by using periodic fine patterns introduced into the excitation light path of a widefield microscope [60]. The technique has achieved a lateral resolution increase by a factor of 2 [61]. STED uses two laser beams; the first is a focused excitation laser that excites the fluorophores, and the second laser with doughnut-shaped intensity profile (or PSF) depletes the excitation of the fluorophores around the excitation spot. This systematically reduces the PSF size leading to increased resolution, up to 20 nm laterally and 30–40 nm axially [62]. SMLM focuses on algorithm-based determination of the precise location of a fluorescent molecule of a known size using PSF statistics. SMLM techniques include photoactivation localization microscopy (PALM) [63], fluorescent PALM (FPALM) [64], PALM with independently running acquisition (PALMIRA) [65] and stochastic optical reconstruction microscopy (STORM) [66]. The basic principle behind these techniques is the sequential and stochastic photoswitching of fluorophores or fluorescent proteins. Only a few fluorophores are switched on, imaged and localised per cycle, ensuring that the probability of having two or more overlapping PSFs is minimised. Consequently, the final super-resolved image is generated through the summation of thousands of acquired image frames.

Here, we describe a super-resolution microscopy approach to unravel the nanostructure of tripartite synapses. Our approach is based on the SMLM method direct STORM (dSTORM) which uses conventional fluorophore-labelled antibodies [67–69]. With this approach we are able to reconstruct the nanoscale localisation of individual astrocytic glutamate transporter (GLT-1) molecules surrounding presynaptic (bassoon) and postsynaptic (Homer1) protein localisations in fixed mouse brain sections.

2. Material and methods

Astrocytic nanoscopy with dSTORM entails tissue acquisition, preparation and processing as well as image acquisition, processing and analysis. The technique relies on tagging a molecule of interest with a fluorescent probe using antibodies. The fluorescence emission of the tag is then captured and its size and location are used as surrogates for the molecule of interest.

2.1. Optical set-up

Super-resolution images were recorded with a Vutara 350 commercial microscope (Bruker Corp., Billerica, US-MA) equipped with the SML biplane technology [70,71]. The machine features two cameras: an Orca Flash 4.0 scientific complementary metal-oxide semiconductor (sCMOS) camera (Hamatasu) with frame rate at 50 Hz for capturing super-resolution images and a semiconductor charge-coupled devices (CCD) camera (Photometrics) used for standard widefield imaging. Images were recorded using a 60x-magnification, 1.2-NA water immersion objective (Olympus). Also used are excitation lasers: 647 nm (for Alexa 647), 561 nm (for CF568) and 488 nm (for Atto 488) and a 405 nm activation laser.

Commercial systems are also available from several other suppliers, for example NIKON and Zeiss, and many home-built systems including lower-cost options have been used for SMLM [72,73]. Our configuration of the Bruker Vutara system does not offer changing the angle of illumination and uses standard epifluorescent illumination. However, changing the angle of illumination can increase contrast and hence many super-resolution imaging systems use total internal reflection (TIR) illumination (when imaging cells) or highly inclined and laminated optical sheet (HILO) illumination (when imaging thicker samples) [74]. In addition to the biplane method of 3D imaging other methods exist [74], for example astigmatism [75], double-helically arranged PSFs [76,77] or interferometry [78]. Astigmatism is the most widely used method to achieve 3D capability. It offers a working range of 1 μm, which is similar to that achieved with biplane [70,77]. On the other hand, double-helix approaches have a usable range of around 2 μm [77], potentially making it the method of choice for non-commercial set-ups.

2.2. Calibration and experimental PSF generation

For the analysis of the SMLM raw data it is helpful to generate an experimental PSF function instead of using a theoretical PSF to 1) fit the fluorophore localisations and 2) calibrate chromatic aberrations and align the individual channels. The experimental PSFs for the laser lines/

fluorophores used can be generated by means of a TetraSpeck bead sample (Thermo, #T7279).

To prepare the calibration sample 1 μl TetraSpeck microspheres are sonicated for 10 min. 500 μl of water is added, the tube vortexed, sonicated again for 10 min and then vortexed again. Next, 100 μl poly-DL-lysine solution (1 mg/ml; Sigma, #P9011) is added to the centre of a No. 1.5 coverglass (for example: SLS #MIC3350; same quality and thickness as the coverslips used for imaging). After 10 min the lysine solution is aspirated and the coverslip air dried completely. 10–30 μl of the prepared 1:500 bead sample are pipetted onto the centre of the dried lysine spot and let stand for 10 min, then aspirated and the sample air dried completely. Finally, 3–5 μl water or Zeiss Immersol W 2010 is pipetted onto a glass slide (e.g. Henso, #7107) and the coverslip is inverted on top. The coverslip is then sealed with nail polish. The bead sample can also be used unmounted with a circular stage adaptor (Thermo, #A7816) and can be stored in phosphate-buffered saline (PBS, Sigma, #4417) at 4 °C. The imaging should also take place in PBS. To generate the experimental PSFs, a z stack (fifty 100 nm steps) of the TetraSpeck sample is imaged and the resulting PSFs are calculated.

2.3. Tissue acquisition

Here, we are using tissue from naïve animals. However, the method is easily adaptable for transgenic animals etc. It is crucial that all animal procedures be carried out in accordance with institutional and local government guidelines, with diligent consideration of the animal's welfare at each step throughout. Animal procedures were conducted as mandated by the European Commission Directive (86/609/EEC) and the United Kingdom Home Office (Scientific Procedures) Act (1986). The images shown here were taken from three P160 (postnatal day 160) male C57BL/6J mice (Charles River, UK). When imaging older animals one has to keep in mind that tissue autofluorescence increases with age [79,80]. As with all imaging approaches, a good signal to noise ratio with as little unwanted fluorescence as possible is crucial for the quality of the resulting image (see below).

Perfusion was performed to cleanse the tissue from auto-fluorescing blood cells. Here, we describe the steps necessary for imaging of resliced 'acute' brain sections that can for be used for electrophysiological examination for instance. Nevertheless, the tissue can also be perfused with fixative directly and then sliced, stained and imaged. The animal was terminally anaesthetised with pentobarbital (i.p., 100 mg/kg; Merial, #R0270A) and laid supine. Testing the paw reflex ensured a stable and deep anaesthesia before continuing. Then, we exposed the pleural cavity, lifted away the sternum and freed the heart from surrounding connective tissue. We inserted a 26-gauge needle into the left ventricle, cut the right atrium and exsanguinated the animal with 10 ml PBS (stored at room temperature). Then, the brain was removed, the appropriate brain regions was dissected out and the brain was sectioned into 350 μm coronal sections using a vibratome (Leica, #VT1000S) (Fig. 1, A). These acute brain sections can be used for immediate live cell examination, or fixed and resliced for immunolabelling. For the fixation, the brain sections were incubated in pre-warmed (37 °C) 4% (w/v) paraformaldehyde (PFA, Sigma, #P6148, stored at 4 °C) in PBS for 30 min at 37 °C. Thereafter, the brain sections were washed three times for 20 min each with PBS. For reslicing, brain sections were flattened out on a glass slide on ice (Fig. 1, B). To immobilise the tissue during reslicing the brain sections were cast into 2% agarose (Lonza, #98200) in PBS (Fig. 1, C). We use small moulds that just fit around the brain sections. With the help of a needle, the brain/agarose block was removed from the mould (Fig. 1, D) and glued to the vibratome stage (Fig. 1, E). Care was taken to prevent any adhesive contacting the area to be sectioned. The tissue was then sectioned into 30 μm coronal sections (Fig. 1, F) and immediately used for immunohistochemistry or stored in PBS supplemented with 0.01% (w/v) sodium azide (NaN₃; Sigma, #S2002) and 100 mM glycine (Sigma, #G8898) at 4 °C. The sodium azide was added to avoid contamination and the glycine was

used to quench autofluorescence from residual fixatives.

When direct tissue labelling is desired, the mouse was first transcardially perfused with PBS as described above, followed by perfusion with 20 ml 4% PFA in PBS, noting the onset of fixation tremors. Good quality perfusion is necessary for good tissue preservation. After perfusion, the brain was removed and post-fixed overnight before being washed thrice with PBS to remove residual PFA. Fixed brains can be stored in PBS supplemented with 0.01% (w/v) sodium azide and 100 mM glycine at 4 °C for up to 3 months prior to sectioning.

The brain was then sectioned using a vibratome. First, we glued a block of 4% agarose in PBS to the vibratome stage and then glued the brain next to the agarose, to secure it during sectioning. Again, care was taken to avoid adhesive contacting the tissue. The brain was then sectioned into 30 μm coronal sections and immediately used for immunohistochemistry or stored in PBS supplemented with 0.01% (w/v) NaN₃ and 100 mM glycine at 4 °C. We recommend using free-floating sections over cryosections in order to facilitate imaging in photoswitching buffer (see below) on inverted microscopes. The free floating sections can be mounted in stage adaptors and imaged in photoswitching buffer to achieve optimal blinking of the fluorophores for SMLM. Cryosections can be used but special isolators (e.g. Sigma, #S0810) have to be used to allow sealing of the tissue in buffer and inversion on top of the objective.

2.4. Tissue labelling

We used immunohistochemistry to label the astrocytic and neuronal proteins. All steps described here were performed gently rocking at room temperature (~21 °C) unless stated otherwise. Brain sections were briefly washed in PBS to remove any residual PFA. Then, they were incubated in 0.1% (w/v) NaBH₄ (Sigma, #71320) in PBS (made fresh on the day) for 15 min to quench autofluorescence from residual free aldehydes [79,81]. Glycine or NH₄Cl can also be used for the quenching. Thereafter, sections were washed thrice for 5 min with PBS. As mentioned, tissue autofluorescence increases with ageing [79,80]. In particular, the fluorescence from lipofuscin, a natural by-product of lysosomal activity in cells interferes with imaging as its emission spectrum overlaps with widely used fluorophores [79,80]. To quench this tissue autofluorescence the sections were treated with 10 mM CuSO₄ (Sigma, #C8027) in 50 mM NH₄Cl (Sigma, #254134) (final pH = 5, stored at room temperature) for 10 min [82]. Another commonly used quencher is sudan black B. However, it introduces autofluorescence in the near infrared channel [83,84] which interferes with the super-resolution imaging (see below). After quenching, the sections were washed quickly with deionised water, followed by three washes with PBS (5 min each).

Permeabilisation and blocking of the tissue was carried out using blocking buffer (PBS supplemented with 0.1% (w/v) saponin (PBS-S; Bio Basic, #SB4521) and 3% (w/v) bovine serum albumin (BSA; Sigma #A7906) for at least three hours. The blocking buffer can be made up in advance and stored at 4 °C for several days. Saponin is an amphipathic glycoside acting as a mild detergent. It reversibly permeabilises the cells by interacting with cholesterol and therefore has to be added throughout the staining process [85]. We recommend the use of glycosides such as saponin (at 0.1%) or digitonin (at 0.1%) when membrane proteins are to be imaged as the commonly used detergents triton X-100 (at 0.1–1%) and Tween 20 (at 0.2%) are non-selective and may remove proteins together with lipids [86]. To prevent unspecific binding of the antibodies we used BSA. Nonetheless, serum (recommended is serum from the animal in which the secondary antibody was raised), milk powder or other blocking agents can be used.

The brain sections were then treated with primary antibodies (Table 1) in PBS-S supplemented with reduced concentration of blocking agent (1% (w/v) BSA) overnight at 4 °C. This incubation step can also be performed at room temperature for only a few hours. Samples were washed briefly with PBS-S (~1 min) and then with PBS-S
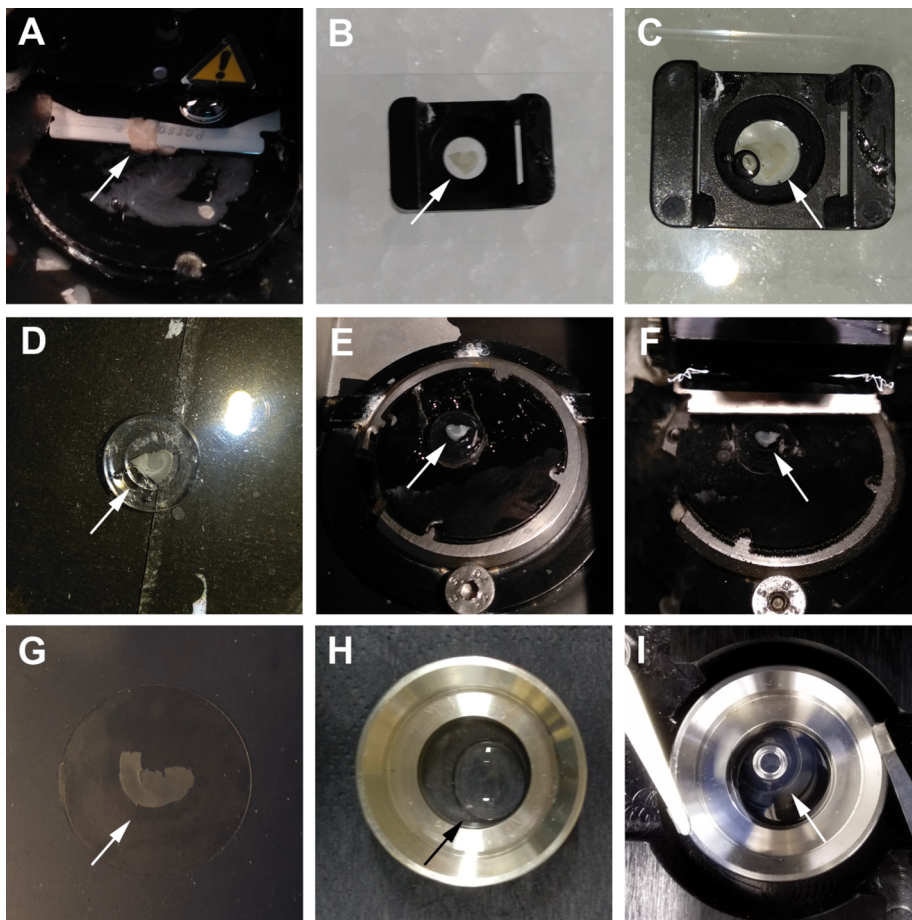
Fig. 1. Tissue preparation for super-resolution imaging. (A) Acute, 350 μm brain sections are cut from a P160, male C57BL/6J mouse using a vibratome. (B) The sections are flattened out on a glass slide on ice. (C) 2% melted agarose is used to immobilise the tissue during reslicing. (D and E) The embedded tissue is glued to a vibratome stage. (F) The tissue is resliced into 30 μm sections. (G) For imaging, brain sections are placed on top of a coverslip. (H) Melted 2% agarose is used to immobilize the tissue. (I) The imaging chamber is filled with buffer, a coverslip is used to seal the chamber and the chamber is placed into the microscope for imaging. The arrows are pointing towards the tissue.

thrice for 10 min to remove surplus primary antibody. Afterwards, the sections were incubated with fluorescently-labelled secondary antibodies (Table 1) diluted in PBS-S for two hours. The best dye to use for SMLM is Alexa 647 (or Cy5) [87,88]. It has excellent photoswitching characteristics and emits in the far-red spectrum, where tissue autofluorescence is comparatively low. For dual labelling Alexa 647 should be used in combination with CF568. Depending on the microscope system, Cy3B or Alexa 568 or Alexa 555 can be used instead. For triple labelling, Atto 488 should be used. Alexa 750 and DyLight 750 have also been used successfully [87,89] but 750 nm lasers are not normally used in commercial microscopes. Different fluorophores display different blinking behaviour and the quality of reconstruction depends on

the number of photons emitted in every photoswitching event. Commercially available antibodies are usually tagged with more than one fluorophore and not all fluorophores will 'blink' so that one cannot reliably estimate the number of actual molecules imaged. To avoid bleaching of the fluorophores, the sections have to be shielded from light (for example using aluminium foil to wrap the plate) from this point on. To avoid bleaching of overexpressed fluorescent proteins the brain sections should be kept covered in aluminium foil from the beginning. After incubation with the secondary antibodies, the sections were washed with PBS-S twice for 10 min and thrice with PBS for 5 min. Lastly, the sections were post-fixed using 4% PFA in PBS for 30 min to immobilize the antibodies in place to avoid movement and hence

Table 1

Antibodies used. Ig = Immunoglobulin, RRID = Research Resource Identifier.

Primary antibodies used						
Antigen	Clone	Host	Supplier	Product code	RRID	Dilution
Bassoon	SAP7F407	Mouse	Novus	NB120-13249	AB_788125	1:250
GLT-1	Polyclonal	Guinea Pig	Merck	AB1783	AB_90949	1:500
Homer1	Polyclonal	Rabbit	Synaptic systems	160 003	AB_887730	1:250

Secondary antibodies used						
Antigen	Feature	Host	Supplier	Product code	RRID	Dilution
Guinea pig IgG	Alexa 647-conjugated	Donkey	Jackson	706–606-148	AB_2340477	1:500
Mouse IgG	CF568-conjugated	Donkey	Biotium	20,105	AB_10557030	1:250
Rabbit IgG	Atto 488-conjugated	Donkey	Sigma	36,098	AB_1137643	1:250

mislocalisations during imaging. This is followed by washing with PBS thrice for 10 min. Sections were stored covered in Scale U2 buffer [4 M urea (Sigma, #U6504), 30% (v/v) glycerol (Fisher, #BP229-1) and 0.1% (v/v) Triton X-100 (Sigma, #T9284)] [90] at 4 °C. This buffer clears the tissue to minimise autofluorescence. Scale U2 buffer can be prepared in advance and stored at 4 °C.

One has to keep in mind that the protocol described here uses complexes of primary and secondary antibodies, and the detected signals represent the position of the fluorophores rather than of the labelled proteins. Strategies exist to reduce this localisation precision error such as tagging primary antibodies directly with fluorophores, or using smaller antibody fragments such as nanobodies [91], aptamers [92], monomeric streptavidin [93] or the pore-forming bacterial toxin streptolysin O [94,95]. Furthermore, the protein of interest can be modified with much smaller tags, using *hexa*-histidine [96,97] or click chemistry approaches [98–100].

2.5. Imaging protocol

Just prior to imaging, the tissue is set atop a No. 1.5 coverslip (25 mm in diameter, SLS #MIC3350) and let to dry slightly (Fig. 1, G). Then, the coverslip is inserted into a 25 mm circular stage adaptor. Melted 2% agarose is pipetted on top of the tissue to immobilize the brain sections on the coverslip (Fig. 1, H). Then, the imaging chamber is filled with switching buffer (~1 ml). The buffer can penetrate the porous agarose gel and hence the tissue. Then a smaller coverslip (18 mm diameter) is set on top to seal the chamber (Fig. 1, I) which is then placed onto the microscope.

The switching buffer is needed to enable 'blinking' of the fluorescent dyes. It usually contains thiols such as mercaptoethylamine (MEA) or β-mercaptoethanol (β-ME) and oxygen scavenging enzymes such as glucose oxidase and catalase [66,87,101]. In multicolour experiments, different fluorophores might require slight changes to the imaging buffer [87,88]. To increase the photoswitching efficiency chemicals such as cyclooctate-traene (COT) [102,103] or Oxyfluor [104] can be added. Moreover, imaging can also be performed in mounting media such as Vectashield [103]. Here, we use a buffer protocol [105] containing 100 mM cysteamine and oxygen scavengers (glucose oxidase and catalase) as well as tris (2-carboxyethyl) phosphine (TCEP), which has been shown to reversibly

quench cyanine dyes for improved photoswitching [106] (Table 2). The increased viscosity of the buffer due to the addition of glycerol leads to diminished interactions of the fluorophores and oxygen [107].

As a first step, a region of interest is selected by scanning the sample in standard epifluorescence mode using the CCD camera. Then, the sCMOS camera is used to confirm the region for super-resolution imaging. Now, the laser power is greatly increased to 0.6–6 mW/μm^2 to induce photo-switching of the fluorophores. Sparse switching of fluorophores is desired to avoid overlapping PSFs. An image series of several thousand (usually 5,000–20,000) frames is recorded until most of the fluorophores have been documented and blinking is diminished. To maximise signal-to-noise ratio and to not split the blinking over multiple frames the exposure/recording time should on average match the time a single fluorophore emits photons - usually between 10 and 30 ms [108,109]. To avoid bleaching and activating the other fluorophores recording should start in the red range of the spectrum and end in the blue range.

2.6. Image analysis

As mentioned, the acquired raw data consists of thousands of frames and up to millions of PSFs. During the analysis, the 3D position of every emitted organic dye is determined as accurately as possible. Most localisation algorithms fit a two- or three-dimensional Gaussian distribution at the centre of every detected fluorophore position and then sample the surrounding pixels [110,111]. Here, we used the Vutara SRX software (version SRX 6.02.05). However, many freely available software packages, e.g. QuickPALM [112] or ThunderSTORM [113] exist also.

We used an in-house analysis suite run in MATLAB (version 2019a; MathWorks, Natick, US-MA) to identify synapses as opposing (within 500 nm) clusters of bassoon and Homer1. We also determined the nearest neighbour distances of GLT-1 molecules surrounding the identified synapses within a radius of 500 nm from the synapse center. The analysis suite is available for download (https://github.com/zhengkaiyu/LocSupRes). Moreover, we used Vutara SRX for cluster analysis of the bassoon and Homer1 localisations using DBScan and a minimum of 50 localisations per cluster and a maximum distance of 100 nm between localisations. We used GraphPad Prism (version 5.01; GraphPad Software, San Diego, US-CA) to plot the distances.

Table 2
Photoswitching buffer [85].

Enzyme Stock Solution (A)		
Ingredient	Concentration	Supplier and product number
10 µl catalase	20 µg/ml	Sigma, #C40
20 µl 1 M TCEP	4 mM	Sigma, #C4706
2.5 ml glycerol	50%	Fisher, #BP229-1
125 µl 1 M KCl	25 mM	Sigma, #P9333
100 µl 1 M Tris- HCl pH 7.5	20 mM	Sigma, #33742
5 mg glucose oxidase	1 mg/ml	Sigma, #G2133
Top up to 5 ml with distilled water and dispense into 50 µl aliquots and store frozen at −20 °C (for up to one year).		

Glucose Stock Solution (B)		
Ingredient	Concentration	supplier and product number
4 g glucose	100 mg/ml	Sigma, #G8270
4 ml glycerol	10%	Fisher, #BP229-1
Top up to 40 ml with distilled water and dispense into 400 µl aliquots and store at −20 °C (for up to one year).		

Reducing Agent Stock Solution (C)		
Ingredient	Concentration	supplier and product number
113.6 mg MEA-HCl	1 M	Sigma, #M6500
Top up to 1 ml with distilled water and store at 4 °C on the day of imaging. This solution can also be prepared in advance and stored at −20 °C for up to one year (do not refreeze).		

Just prior to imaging the above solutions are mixed:
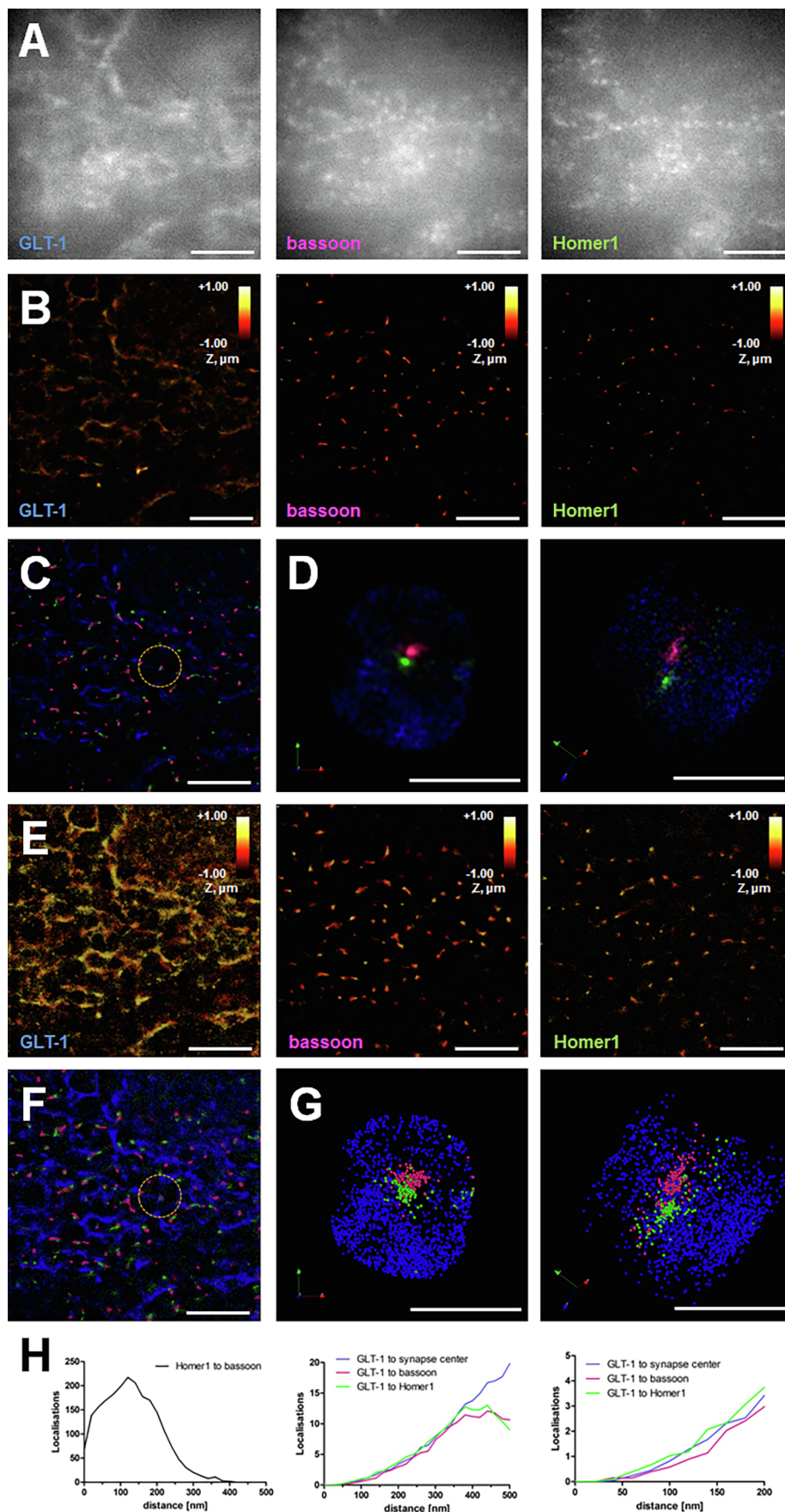50 µl Solution A, 400 µl Solution B, 100 µl Solution C, 450 µl PBS.

Fig. 2. Super-resolution imaging of tripartite synapses in fixed mouse brain sections. (A) Wide-field images of astrocytic glutamate transporter GLT-1 (A1) and presynaptic protein bassoon (A2) and postsynaptic protein Homer1 (A3) in hippocampal CA1 area *stratum radiatum* in a fixed mouse 30 μm brain section (P160 male C57BL/6J). (B) 3D three-color dSTORM super-resolution imaging: Snapshots of molecular patterns for astrocytic GLT-1 (Alexa 647, B1), presynaptic bassoon (CF568, B2) and postsynaptic Homer1 (Atto 488, B3). The images are colour-coded according to the z position of the molecules in a 2 μm deep stack. (C) Merged image of images shown in B; GLT-1 (blue), bassoon (magenta) and Homer1 (green). Displayed are 2D projections of 3D SMLM molecular maps; label brightness reflects molecular density. (D) Close-up on the highlighted area in C; two viewing angles shown. (E) Same images as in B but as cloud representations of localised molecules with a constant diameter of 30 nm. (F) Merged image of images shown in E. (G) Close-up on the highlighted area in F; two viewing angles shown. (H) Nearest-neighbour distances (<500 nm) between synaptic molecules bassoon and Homer1 (H1). Distances of GLT-1 molecules to the center of identified synapses, bassoon or Homer1 molecules (H2). A zoomed in view of the distances up to 200 nm highlights that more GLT-1 molecules are closer to Homer1 than to bassoon or to the synapse center (H3). Scale bars = 5 μm (A-C and E-F) and 1 μm (D and G). (For interpretation of the references to color in this figure legend, the reader is referred to the web version of this article.)

3. Results and discussion

Here, we describe a protocol for super-resolution imaging of tripartite synapses. We use the well described marker proteins piccolo for presynaptic structures, PSD95 for postsynaptic specialisations and GLT-1 as a marker of astrocytic membranes.

After immunostaining, the tissue was prepared for super-resolution imaging and placed into the imaging chamber in photoswitching buffer. First, epifluorescence images of all three proteins were taken to identify the region of interest (Fig. 2, A). We imaged tripartite synapses in the CA1 *stratum radiatum* area of mouse hippocampus. The epifluorescence images show diffuse labelling with the GLT-1 antibody with some clustering throughout the neuropil, similar to what we and others have published before [50]. The synaptic molecules bassoon and Homer1 are scattered throughout the imaged tissue, forming clusters with roughly 1 μm distance between them [114]. After increasing the laser power, the 'blinking' of the fluorophores was registered and the final super-resolved images were generated (Fig. 2, B). The super-resolution images show the same area as in Fig. 2, A. Super-resolution microscopy revealed clusters of GLT-1, bassoon and Homer1 that were hardly identifiable in the epifluorescence images. Fig. 2, C is the merged image of the three super-resolved images in Fig. 2, B. Synapses are revealed with presynaptic (magenta) and postsynaptic (green) sites spaced apart from each other, revealing the synaptic cleft between them. The GLT-1 molecules (blue) form 'clouds' surrounding synapses with some clustering close to the synaptic molecules. The circled area in Fig. 2, C is depicted in two rotated views in Fig. 2, D. Presynaptic bassoon molecules are opposing postsynaptic Homer1 molecules. Surrounding the synapse are 'clouds' of GLT-1 molecules. Fig. 2, E–G represent the same images as in Fig. 2, B–D but the localisations are visualised as point clouds with a constant diameter of 30 nm. We measured the nearest neighbour

distances of synaptic localisations in the area imaged (Fig. 2, H). We chose 500 nm as the cut-off point as it roughly represents the halfway point between two neighbouring synapses. The obersavation frequency for distances between bassoon and Homer1 localisations peaks at 120 nm (Fig. 2, H), a distance similar to published series [115]. The variety in distances might be due to activity states of the individual synapses in addition to mislocalisations and variation in labelling and imaging. GLT-1 molecules appear a little bit closer to the postsynaptic molecule Homer1 than they are to the presynaptic molecule bassoon or the synapse center (Fig. 2, H2 and H3).

We performed cluster analyses of the bassoon and Homer1 molecules across three imaged brain sections. We chose a minimum of 50 localisations per cluster and a maximum distance between two nearest neighbours of 100 nm as inclusion criteria. The analysis identified 84 synapses (distance between bassoon and Homer1 cluster center points less than 500 nm). Fig. 3 shows the identified clusters for bassoon (A) and Homer1 (B) represented as cluster hulls. Fig. 3, C is the same synapse highlighted in Fig. 2. Both, bassoon and Homer1, form clusters with varying numbers of localisations and resulting cluster volumes and densities, with small clusters being dominant (Fig. 3, D). As mentioned above, the number of localisations does not necessarily correspond to the actual number of molecules present. The different fluorophores behave differently in the buffer system, increasing the difficulty of multi-colour imaging.

4. Conclusion

The method described here details a super-resolution microscopy approach to image tripartite synapses on the nanoscale. The protocol is easily adapted to any three-colour imaging and can be used in a wide range of biological applications. Super-resolution imaging has allowed discoveries of the arrangement of cytoskeleton in axons, dendritic spine
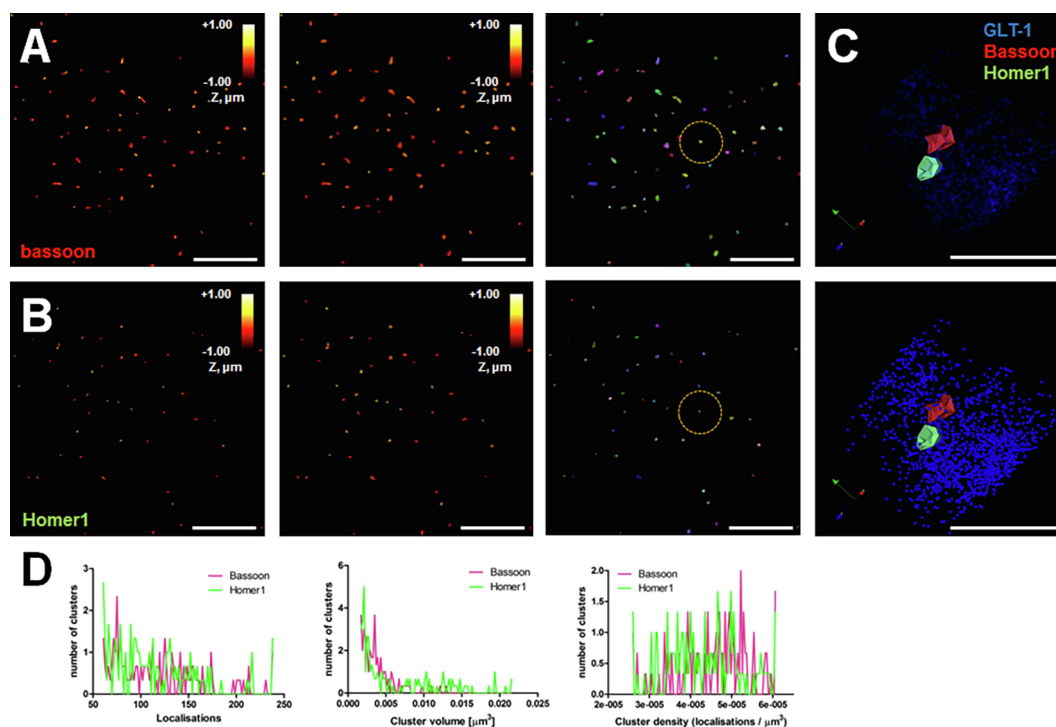

Fig. 3. Cluster analysis of super-resolved synaptic molecules. (A) Clusters of super-resolved bassoon molecules in hippocampal CA1 area *stratum radiatum* in a fixed mouse 30 μm brain section (P160 male C57BL/6J) as in Fig. 2. The clusters are colour-coded according to the z position of the molecules in a 2 μm deep stack (A1 and A2) and visualised as cluster hulls as point splatted (A1), as point clouds (A2) and colour-coded as different as different clusters. **(B)** Clusters of super-resolved Homer1 molecules represented as in A. (C) Close-up of area highlighted in A and B. GLT-1 molecules (blue) surrounding the opposing synaptic molecules (bassoon in red and Homer1 in green) Merged image of images shown in B; GLT-1 (blue), bassoon (magenta) and Homer1 (green). Displayed are 2D projections of 3D SMLM molecular maps; label brightness reflects molecular density. (D) Cluster analysis on 84 synapses, depicting the number of localisations per cluster, the cluster volume and the density of localisations within the clusters. Scale bars = 5 μm (A and B) and 1 μm (C). (For interpretation of the references to color in this figure legend, the reader is referred to the web version of this article.)

plasticity and molecular arrangements in pre- and postsynaptic specialisations [50,116,117]. Super-resolution imaging has increased our knowledge not only in fixed preparations but also in living brain slices [118] and living and freely behaving animals [119–121]. These techniques offer resolution far below that achieved with conventional microscopy techniques. Previously this was only possible with the help of 3D EM; a method that is costlier, technically demanding, time-consuming and does not allow imaging of living cells or animals. Here, we measured the distances between individual astrocytic and neuronal molecules. We found GLT-1 molecules located throughout the neuropil with some in close proximity to synapses as has been seen with conventional microscopy and EM [122]. Although morphological data cannot readily be obtained with SMLM it offers multi-colour imaging and easier 3D capabilities over a range of several microns. Glia cells have not seen a great deal of interest in the super-resolution field but with the advent of more convenient methodologies we will learn more about their functions in the healthy brain and what can go wrong in disease.

5. Equipment and supply list

5.1. Chemicals

Material	Purpose	Provider
Antibodies	Immunochemistry	See Table 1
Agarose	Tissue immobilisation	Lonza, #98200
BSA	Blocking of unspecific antibody binding	Sigma #A7906
Catalase	Photoswitching buffer	Sigma, #C40
CuSO$_4$	Quenching tissue autofluorescence	Sigma, #C8027
glucose	Photoswitching buffer	Sigma, #G8270
glucose oxidase	Photoswitching buffer	Sigma, #G2133
Glycerol	Tissue clearing, photoswitching buffer	Fisher, #BP229-1
Glycine	Quenching fixative autofluorescence	Sigma, #G8898
KCl	Photoswitching buffer	Sigma, #P9333
MEA-HCl	Photoswitching buffer	Sigma, #M6500
NaBH$_4$	Quenching fixative autofluorescence	Sigma, #71320
NaN$_3$	Tissue preservation	Sigma, #S2002
NH$_4$Cl	Quenching fixative autofluorescence	Sigma, #254134
PBS	Buffer	Sigma, #4417
PFA	Fixation of brain and slices	Sigma, #P6148
Pentobarbital (Euthatal)	Anaesthesia	Merial, #R0270A
Poly-DL-lysine	Coverslip coating to improve adhesion	Sigma, #P9011
Saponin	Permeabilisation of cell membrane	Bio Basic, #SB4521
TCEP	Photoswitching buffer	Sigma, #C4706
Tris-HCl	Photoswitching buffer	Sigma, #33742
Triton X-100	Tissue clearing	Sigma, #T9284
Urea	Tissue clearing	Sigma, #U6504

5.2. Supply list

Material	Purpose	Provider
Coverslips	Tissue immobilisation	SLS, #MIC3350
Glass slides	PSF calibration	Henzo, #7107
TetraSpeck beads	PSF calibration	Thermo, #T7279

5.3. Equipment

Material	Purpose	Provider
60x, 1.2-NA objective	Imaging	Olympus
Circular stage adaptor	Holds coverslips for imaging	Thermo, #A7816
Lasers	Excitation and activation	Coherent
Orca Flash 4.0 sCMOS camera	super-resolution imaging	Hamatasu
CCD camera	Standard widefield imaging	Photometrics
Vibratome	Brain sectioning	Leica, #VT1000S
Vutara 350 microscope	Imaging	Bruker

5.4. Software

Name	Purpose	Source
GraphPad Prism 5-.01	Data analysis	GraphPad Software
MATLAB 2019a	Data analysis	MathWorks
Vutara SRX 6.02.05	Single molecule image acquisition and analysis	Bruker

Appendix A. Supplementary data

Supplementary data to this article can be found online at https://doi.org/10.1016/j.ymeth.2019.05.024.

References

[1] A. Araque, G. Carmignoto, P.G. Haydon, S.H. Oliet, R. Robitaille, A. Volterra, Gliotransmitters travel in time and space, Neuron 81 (4) (2014) 728–739.
[2] T. Deemyad, J. Luthi, N. Spruston, Astrocytes integrate and drive action potential firing in inhibitory subnetworks, Nat. Commun. 9 (1) (2018) 4336.
[3] M. Santello, N. Toni, A. Volterra, Astrocyte function from information processing to cognition and cognitive impairment, Nat. Neurosci. 22 (2) (2019) 154–166.
[4] E.A. Bushong, M.E. Martone, Y.Z. Jones, M.H. Ellisman, Protoplasmic astrocytes in CA1 stratum radiatum occupy separate anatomical domains, J. Neurosci. 22 (1) (2002) 183–192.
[5] E.A. Bushong, M.E. Martone, M.H. Ellisman, Maturation of astrocyte morphology and the establishment of astrocyte domains during postnatal hippocampal development, Int. J. Dev. Neurosci. 22 (2) (2004) 73–86.
[6] M.M. Halassa, T. Fellin, H. Takano, J.H. Dong, P.G. Haydon, Synaptic islands defined by the territory of a single astrocyte, J. Neurosci. 27 (24) (2007) 6473–6477.
[7] B.S. Khakh, M.V. Sofroniew, Diversity of astrocyte functions and phenotypes in neural circuits, Nat. Neurosci. 18 (7) (2015) 942–952.
[8] J.P. Heller, D.A. Rusakov, Morphological plasticity of astroglia: Understanding synaptic microenvironment, Glia 63 (12) (2015) 2133–2151.
[9] A. Verkhratsky, M. Nedergaard, Physiology of astroglia, Physiol. Rev. 98 (1) (2018) 239–389.
[10] T.M. Mathiisen, K.P. Lehre, N.C. Danbolt, O.P. Ottersen, The perivascular astroglial sheath provides a complete covering of the brain microvessels: an electron microscopic 3D reconstruction, Glia 58 (9) (2010) 1094–1103.
[11] M. Nedergaard, Neuroscience. Garbage truck of the brain, Science 340 (6140) (2013) 1529–1530.
[12] B.A. MacVicar, E.A. Newman, Astrocyte regulation of blood flow in the brain, Cold Spring Harb. Perspect. Biol. 7 (5) (2015).
[13] L.F. Barros, B. Weber, CrossTalk proposal: an important astrocyte-to-neuron lactate shuttle couples neuronal activity to glucose utilisation in the brain, J. Physiol. 596 (3) (2018) 347–350.
[14] L. Hertz, J. Xu, D. Song, T. Du, B. Li, E. Yan, L. Peng, Astrocytic glycogenolysis: mechanisms and functions, Metab. Brain Dis. 30 (1) (2015) 317–333.
[15] N. Marina, E. Turovsky, I.N. Christie, P.S. Hosford, A. Hadjihambi, A. Korsak, R. Ang, S. Mastitskaya, S. Sheikhbahaei, S.M. Theparambil, A.V. Gourine, Brain metabolic sensing and metabolic signaling at the level of an astrocyte, Glia 66 (6) (2018) 1185–1199.
[16] M.M. Halassa, C. Florian, T. Fellin, J.R. Munoz, S.Y. Lee, T. Abel, P.G. Haydon, M.G. Frank, Astrocytic modulation of sleep homeostasis and cognitive consequences of sleep loss, Neuron 61 (2) (2009) 213–219.
[17] N.J. Allen, D.A. Lyons, Glia as architects of central nervous system formation and function, Science 362 (6411) (2018) 181–185.
[18] W.S. Chung, N.J. Allen, C. Eroglu, Astrocytes control synapse formation, function, and elimination, Cold Spring Harb. Perspect. Biol. 7 (9) (2015) a020370.
[19] M. De Pitta, N. Brunel, A. Volterra, Astrocytes: Orchestrating synaptic plasticity? Neuroscience 323 (2016) 43–61.
[20] D.A. Coulter, T. Eid, Astrocytic regulation of glutamate homeostasis in epilepsy, Glia 60 (8) (2012) 1215–1226.
[21] U. Lichter-Konecki, J.M. Mangin, H. Gordish-Dressman, E.P. Hoffman, V. Gallo,

Gene expression profiling of astrocytes from hyperammonemic mice reveals altered pathways for water and potassium homeostasis in vivo, Glia 56 (4) (2008) 365–377.

[22] C. Murphy-Royal, J. Dupuis, L. Groc, S.H.R. Oliet, Astroglial glutamate transporters in the brain: regulating neurotransmitter homeostasis and synaptic transmission, J. Neurosci. Res. 95 (11) (2017) 2140–2151.

[23] M.L. Olsen, B.S. Khakh, S.N. Skatchkov, M. Zhou, C.J. Lee, N. Rouach, New insights on astrocyte ion channels: critical for homeostasis and neuron-glia signaling, J. Neurosci. 35 (41) (2015) 13827–13835.

[24] V. Parpura, A. Verkhratsky, Neuroglia at the crossroads of homoeostasis, metabolism and signalling: evolution of the concept, ASN Neuro 4 (4) (2012) 201–205.

[25] M. Simard, M. Nedergaard, The neurobiology of glia in the context of water and ion homeostasis, Neuroscience 129 (4) (2004) 877–896.

[26] J.E. Burda, M.V. Sofroniew, Reactive gliosis and the multicellular response to CNS damage and disease, Neuron 81 (2) (2014) 229–248.

[27] V. Parpura, M.T. Heneka, V. Montana, S.H. Oliet, A. Schousboe, P.G. Haydon, R.F. Stout Jr., D.C. Spray, A. Reichenbach, T. Pannicke, M. Pekny, M. Pekna, R. Zorec, A. Verkhratsky, Glial cells in (patho)physiology, J. Neurochem. 121 (1) (2012) 4–27.

[28] A. Verkhratsky, M.V. Sofroniew, A. Messing, N.C. deLanerolle, D. Rempe, J.J. Rodriguez, M. Nedergaard, Neurological diseases as primary gliopathies: a reassessment of neurocentrism, ASN Neuro 4 (3) (2012).

[29] X. Han, M. Chen, F. Wang, M. Windrem, S. Wang, S. Shanz, Q. Xu, N.A. Oberheim, L. Bekar, S. Betstadt, A.J. Silva, T. Takano, S.A. Goldman, M. Nedergaard, Forebrain engraftment by human glial progenitor cells enhances synaptic plasticity and learning in adult mice, Cell Stem Cell 12 (3) (2013) 342–353.

[30] N.A. Oberheim, T. Takano, X. Han, W. He, J.H. Lin, F. Wang, Q. Xu, J.D. Wyatt, W. Pilcher, J.G. Ojemann, B.R. Ransom, S.A. Goldman, M. Nedergaard, Uniquely hominid features of adult human astrocytes, J. Neurosci. 29 (10) (2009) 3276–3287.

[31] M.S. Windrem, S.J. Schanz, C. Morrow, J. Munir, D. Chandler-Militello, S. Wang, S.A. Goldman, A competitive advantage by neonatally engrafted human glial progenitors yields mice whose brains are chimeric for human glia, J. Neurosci. 34 (48) (2014) 16153–16161.

[32] T.A. Jones, W.T. Greenough, Ultrastructural evidence for increased contact between astrocytes and synapses in rats reared in a complex environment, Neurobiol. Learn. Mem. 65 (1) (1996) 48–56.

[33] G. Salois, J.S. Smith, Housing complexity alters GFAP-immunoreactive astrocyte morphology in the rat dentate gyrus, Neural Plast. 2016 (2016) 3928726.

[34] D.A. Rusakov, Disentangling calcium-driven astrocyte physiology, Nat. Rev. Neurosci. 16 (4) (2015) 226–233.

[35] N. Bazargani, D. Attwell, Astrocyte calcium signaling: the third wave, Nat. Neurosci. 19 (2) (2016) 182–189.

[36] A. Volterra, N. Liaudet, I. Savtchouk, Astrocyte Ca(2)(+) signalling: an unexpected complexity, Nat. Rev. Neurosci. 15 (5) (2014) 327–335.

[37] A. Covelo, A. Araque, Neuronal activity determines distinct gliotransmitter release from a single astrocyte, Elife 7 (2018).

[38] S. Mederos, C. Gonzalez-Arias, G. Perea, Astrocyte-neuron networks: a multilane highway of signaling for homeostatic brain function, Front. Synaptic Neurosci. 10 (2018) 45.

[39] L. Schermelleh, A. Ferrand, T. Huser, C. Eggeling, M. Sauer, O. Biehlmaier, G.P.C. Drummen, Super-resolution microscopy demystified, Nat. Cell Biol. 21 (1) (2019) 72–84.

[40] C. Cremer, A. Szczurek, F. Schock, A. Gourram, U. Birk, Super-resolution microscopy approaches to nuclear nanostructure imaging, Methods 123 (2017) 11–32.

[41] J. Spacek, Three-dimensional analysis of dendritic spines. III. Glial sheath, Anat. Embryol. 171 (2) (1985) 245–252.

[42] M.R. Witcher, Y.D. Park, M.R. Lee, S. Sharma, K.M. Harris, S.A. Kirov, Three-dimensional relationships between perisynaptic astroglia and human hippocampal synapses, Glia 58 (5) (2010) 572–587.

[43] K.P. Lehre, D.A. Rusakov, Asymmetry of glia near central synapses favors presynaptically directed glutamate escape, Biophys. J . 83 (1) (2002) 125–134.

[44] N. Gavrilov, I. Golyagina, A. Brazhe, A. Scimemi, V. Turlapov, A. Semyanov, Astrocytic coverage of dendritic spines dendritic shafts, and axonal boutons in hippocampal neuropil, ,Front. Cell Neurosci. 12 (2018) 248.

[45] N.V. Medvedev, C. Popov, I. Henneberger, D.A. Kraev, M.G. Rusakov, Stewart Glia selectively approach synapses on thin dendritic spines, Philos. Trans. R. Soc. London. Ser. B, Biol. Sci. 369 (2014) 1654 20140047.

[46] M. Lavialle, G. Aumann, E. Anlauf, F. Prols, M. Arpin, A. Derouiche, Structural plasticity of perisynaptic astrocyte processes involves ezrin and metabotropic glutamate receptors, PNAS 108 (31) (2011) 12915–12919.

[47] A. Derouiche, M. Frotscher, Peripheral astrocyte processes: monitoring by selective immunostaining for the actin-binding ERM proteins, Glia 36 (3) (2001) 330–341.

[48] K. Hama, T. Arii, E. Katayama, M. Marton, M.H. Ellisman, Tri-dimensional morphometric analysis of astrocytic processes with high voltage electron microscopy of thick Golgi preparations, J. Neurocytol. 33 (3) (2004) 277–285.

[49] J.P. Heller, P. Michaluk, K. Sugao, D.A. Rusakov, Probing nano-organization of astroglia with multi-color super-resolution microscopy, J. Neurosci. Res. (2017).

[50] J.P. Heller, D.A. Rusakov, The nanoworld of the tripartite synapse: insights from super-resolution microscopy, Front. Cell. Neurosci. 11 (2017) 374.

[51] K. Sakers, A.M. Lake, R. Khazanchi, R. Ouwenga, M.J. Vasek, A. Dani, J.D. Dougherty, Astrocytes locally translate transcripts in their peripheral processes, Proc. Nat. Acad. Sci. U. S. A. (2017).

[52] A.J. Smith, A.S. Verkman, Superresolution imaging of aquaporin-4 cluster size in antibody-stained paraffin brain sections, Biophys. J. 109 (12) (2015) 2511–2522.

[53] J. Jorgacevski, M. Potokar, M. Kreft, A. Gucek, J.P. Mothet, R. Zorec, Astrocytic vesicle-based exocytosis in cultures and acutely isolated hippocampal rodent slices, J. Neurosci. Res. (2017).

[54] L.P. Savtchenko, L. Bard, T.P. Jensen, J.P. Reynolds, I. Kraev, N. Medvedev, M.G. Stewart, C. Henneberger, D.A. Rusakov, Disentangling astroglial physiology with a realistic cell model in silico, Nat. Commun. 9 (1) (2018) 3554.

[55] J. Vangindertael, R. Camacho, W. Sempels, H. Mizuno, P. Dedecker, K.P.F. Janssen, An introduction to optical super-resolution microscopy for the adventurous biologist, Methods Appl. Fluoresc. 6 (2) (2018) 022003.

[56] Y.M. Sigal, R. Zhou, X. Zhuang, Visualizing and discovering cellular structures with super-resolution microscopy, Science 361 (6405) (2018) 880–887.

[57] R. Heintzmann, T. Huser, Super-resolution structured illumination microscopy, Chem. Rev. 117 (23) (2017) 13890–13908.

[58] G. Vicidomini, P. Bianchini, A. Diaspro, STED super-resolved microscopy, Nat. Methods 15 (3) (2018) 173–182.

[59] D. Baddeley, J. Bewersdorf, Biological insight from super-resolution microscopy: what we can learn from localization-based images, Annu. Rev. Biochem. 87 (2018) 965–989.

[60] M.G. Gustafsson, Extended resolution fluorescence microscopy, Curr. Opin. Struct. Biol. 9 (5) (1999) 627–634.

[61] M.G. Gustafsson, Surpassing the lateral resolution limit by a factor of two using structured illumination microscopy, J. Microsc. 198 (Pt 2) (2000) 82–87.

[62] S.W. Hell, J. Wichmann, Breaking the diffraction resolution limit by stimulated emission: stimulated-emission-depletion fluorescence microscopy, Opt. Lett. 19 (11) (1994) 780–782.

[63] E. Betzig, G.H. Patterson, R. Sougrat, O.W. Lindwasser, S. Olenych, J.S. Bonifacino, M.W. Davidson, J. Lippincott-Schwartz, H.F. Hess, Imaging intracellular fluorescent proteins at nanometer resolution, Science 313 (5793) (2006) 1642–1645.

[64] S.T. Hess, T.P. Girirajan, M.D. Mason, Ultra-high resolution imaging by fluorescence photoactivation localization microscopy, Biophys. J. 91 (11) (2006) 4258–4272.

[65] A. Egner, C. Geisler, C. von Middendorff, H. Bock, D. Wenzel, R. Medda, M. Andresen, A.C. Stiel, S. Jakobs, C. Eggeling, A. Schonle, S.W. Hell, Fluorescence nanoscopy in whole cells by asynchronous localization of photoswitching emitters, Biophys. J. 93 (9) (2007) 3285–3290.

[66] M.J. Rust, M. Bates, X. Zhuang, Sub-diffraction-limit imaging by stochastic optical reconstruction microscopy (STORM), Nat. Methods 3 (10) (2006) 793–795.

[67] S. van de Linde, A. Loschberger, T. Klein, M. Heidbreder, M. Wolter, M. Heilemann, M. Sauer, Direct stochastic optical reconstruction microscopy with standard fluorescent probes, Nat. Protoc. 6 (7) (2011) 991–1009.

[68] U. Endesfelder, M. Heilemann, Direct stochastic optical reconstruction microscopy (dSTORM), Methods Mol. Biol. 1251 (2015) 263–276.

[69] M. Heilemann, S. van de Linde, M. Schuttpelz, R. Kasper, B. Seefeldt, A. Mukherjee, P. Tinnefeld, M. Sauer, Subdiffraction-resolution fluorescence imaging with conventional fluorescent probes, Angew. Chem. Int. Ed. Engl. 47 (33) (2008) 6172–6176.

[70] M.F. Juette, T.J. Gould, M.D. Lessard, M.J. Mlodzianoski, B.S. Nagpure, B.T. Bennett, S.T. Hess, J. Bewersdorf, Three-dimensional sub-100 nm resolution fluorescence microscopy of thick samples, Nat. Methods 5 (6) (2008) 527–529.

[71] M.J. Mlodzianoski, M.F. Juette, G.L. Beane, J. Bewersdorf, Experimental characterization of 3D localization techniques for particle-tracking and super-resolution microscopy, Opt. Express 17 (10) (2009) 8264–8277.

[72] K. Kwakwa, A. Savell, T. Davies, I. Munro, S. Parrinello, M.A. Purbhoo, C. Dunsby, M.A. Neil, P.M. French, easySTORM: a robust, lower-cost approach to localisation and TIRF microscopy, J. Biophotonics 9 (9) (2016) 948–957.

[73] B. Diederich, P. Then, A. Jugler, R. Forster, R. Heintzmann, cellSTORM-Cost-effective super-resolution on a cellphone using dSTORM, PLoS ONE 14 (1) (2019) e0209827.

[74] S. Herbert, H. Soares, C. Zimmer, R. Henriques, Single-molecule localization super-resolution microscopy: deeper and faster, Microsc. Microanal. 18 (6) (2012) 1419–1429.

[75] H.P. Kao, A.S. Verkman, Tracking of single fluorescent particles in three dimensions: use of cylindrical optics to encode particle position, Biophys. J. 67 (3) (1994) 1291–1300.

[76] S.R. Pavani, M.A. Thompson, J.S. Biteen, S.J. Lord, N. Liu, R.J. Twieg, R. Piestun, W.E. Moerner, Three-dimensional,, single-molecule fluorescence imaging beyond the diffraction limit by using a double-helix point spread function, PNAS 106 (9) (2009) 2995–2999.

[77] M. Badieirostami, M.D. Lew, M.A. Thompson, W.E. Moerner, Three-dimensional localization precision of the double-helix point spread function versus astigmatism and biplane, Appl. Phys. Lett. 97 (16) (2010) 161103.

[78] G. Shtengel, J.A. Galbraith, C.G. Galbraith, J. Lippincott-Schwartz, J.M. Gillette, S. Manley, R. Sougrat, C.M. Waterman, P. Kanchanawong, M.W. Davidson, R.D. Fetter, H.F. Hess, Interferometric fluorescent super-resolution microscopy resolves 3D cellular ultrastructure, PNAS 106 (9) (2009) 3125–3130.

[79] A.S. Davis, A. Richter, S. Becker, J.E. Moyer, A. Sandouk, J. Skinner, J.K. Taubenberger, Characterizing and diminishing autofluorescence in formalin-fixed paraffin-embedded human respiratory tissue, J. Histochem. Cytochem. 62 (6) (2014) 405–423.

[80] Y. Mochizuki, M.K. Park, T. Mori, S. Kawashima, The difference in autofluorescence features of lipofuscin between brain and adrenal, Zoolog. Sci. 12 (3) (1995) 283–288.

[81] B. Clancy, L.J. Cauller, Reduction of background autofluorescence in brain sections following immersion in sodium borohydride, J. Neurosci. Methods 83 (2) (1998) 97–102.

[82] S.A. Schnell, W.A. Staines, M.W. Wessendorf, Reduction of lipofuscin-like auto-fluorescence in fluorescently labeled tissue, J. Histochem. Cytochem. 47 (6) (1999) 719–730.

[83] H.J. Romijn, J.F. van Uum, I. Breedijk, J. Emmering, I. Radu, C.W. Pool, Double immunolabeling of neuropeptides in the human hypothalamus as analyzed by confocal laser scanning fluorescence microscopy, J. Histochem. Cytochem. 47 (2) (1999) 229–236.

[84] W. Baschong, R. Suetterlin, R.H. Laeng, Control of autofluorescence of archival formaldehyde-fixed, paraffin-embedded tissue in confocal laser scanning micro-scopy (CLSM), J. Histochem. Cytochem. 49 (12) (2001) 1565–1572.

[85] M.A. Lacaille-Dubois, H. Wagner, A review of the biological and pharmacological activities of saponins, Phytomedicine 2 (4) (1996) 363–386.

[86] M.C. Jamur, C. Oliver, Permeabilization of cell membranes, Methods Mol. Biol. 588 (2010) 63–66.

[87] G.T. Dempsey, J.C. Vaughan, K.H. Chen, M. Bates, X. Zhuang, Evaluation of fluorophores for optimal performance in localization-based super-resolution ima-ging, Nat. Methods 8 (12) (2011) 1027–1036.

[88] B. Turkowyd, D. Virant, U. Endesfelder, From single molecules to life: microscopy at the nanoscale, Anal. Bioanal. Chem. 408 (25) (2016) 6885–6911.

[89] T. Zhao, Y. Wang, Y. Zhai, X. Qu, A. Cheng, S. Du, M.M. Loy, A user-friendly two-color super-resolution localization microscope, Opt. Express 23 (2) (2015) 1879–1887.

[90] H. Hama, H. Kurokawa, H. Kawano, R. Ando, T. Shimogori, H. Noda, K. Fukami, A. Sakaue-Sawano, A. Miyawaki, Scale: a chemical approach for fluorescence imaging and reconstruction of transparent mouse brain, Nat. Neurosci. 14 (11) (2011) 1481–1488.

[91] T. Pleiner, M. Bates, S. Trakhanov, C.T. Lee, J.E. Schliep, H. Chug, M. Bohning, H. Stark, H. Urlaub, D. Gorlich, Nanobodies: site-specific labeling for super-re-solution imaging, rapid epitope-mapping and native protein complex isolation, Elife 4 (2015) e11349.

[92] M.A. de Castro, B. Rammner, F. Opazo, Aptamer stainings for super-resolution microscopy, Methods Mol. Biol. 1380 (2016) 197–210.

[93] I. Chamma, O. Rossier, G. Giannone, O. Thoumine, M. Sainlos, Optimized labeling of membrane proteins for applications to super-resolution imaging in confined cellular environments using monomeric streptavidin, Nat. Protoc. 12 (4) (2017) 748–763.

[94] K.W. Teng, Y. Ishitsuka, P. Ren, Y. Youn, X. Deng, P. Ge, A.S. Belmont, P.R. Selvin, Labeling proteins inside living cells using external fluorophores for microscopy, Elife 5 (2016).

[95] K.W. Teng, Y. Ishitsuka, P. Ren, Y. Youn, X. Deng, P. Ge, S.H. Lee, A.S. Belmont, P.R. Selvin, Labeling proteins inside living cells using external fluorophores for fluorescence microscopy, Elife 6 (2017).

[96] R. Wieneke, A. Raulf, A. Kollmannsperger, M. Heilemann, R. Tampe, SLAP: small labeling pair for single-molecule super-resolution imaging, Angew. Chem. Int. Ed. Engl. 54 (35) (2015) 10216–10219.

[97] J. Lotze, U. Reinhardt, O. Seitz, A.G. Beck-Sickinger, Peptide-tags for site-specific protein labelling in vitro and in vivo, Mol. BioSyst. 12 (6) (2016) 1731–1745.

[98] P. Mateos-Gil, S. Letschert, S. Doose, M. Sauer, Super-resolution imaging of plasma membrane proteins with click chemistry, Front. Cell Dev. Biol. 4 (2016) 98.

[99] A. Raulf, C.K. Spahn, P.J. Zessin, K. Finan, S. Bernhardt, A. Heckel, M. Heilemann, Click,, chemistry facilitates direct labelling and super-resolution imaging of nu-cleic acids and proteinsdaggerElectronic supplementary information (ESI) avail-able. See DOI: 10.1039/c4ra01027bClick here for additional data file, RSC Adv 4 (57) (2014) 30462–30466 -.

[100] T. Triemer, A. Messikommer, S.M.K. Glasauer, J. Alzeer, M.H. Paulisch, N.W. Luedtke, Superresolution imaging of individual replication forks reveals unexpected prodrug resistance mechanism, PNAS 115 (7) (2018) E1366–E1373.

[101] T.J. Chozinski, L.A. Gagnon, J.C. Vaughan, Twinkle, twinkle little star: photo-switchable fluorophores for super-resolution imaging, FEBS Lett. 588 (19) (2014) 3603–3612.

[102] M. Minoshima, K. Kikuchi, Photostable and photoswitching fluorescent dyes for super-resolution imaging, J. Biol. Inorg. Chem. (2017).

[103] N. Olivier, D. Keller, P. Gonczy, S. Manley, Resolution doubling in 3D-STORM imaging through improved buffers, PLoS ONE 8 (7) (2013) e69004.

[104] L. Nahidiazar, A.V. Agronskaia, J. Broertjes, B. van den Broek, K. Jalink, Optimizing imaging conditions for demanding multi-color super resolution loca-lization microscopy, PLoS ONE 11 (7) (2016) e0158884.

[105] D.J. Metcalf, R. Edwards, N. Kumarswami, A.E. Knight, Test,, samples for opti-mizing STORM super-resolution microscopy, J. Vis. Exp. (79 2013).

[106] J.C. Vaughan, G.T. Dempsey, E. Sun, X. Zhuang, Phosphine quenching of cyanine dyes as a versatile tool for fluorescence microscopy, J. Am. Chem. Soc. 135 (4) (2013) 1197–1200.

[107] E. Johnson, R. Kaufmann, Preserving the photoswitching ability of standard fluorescent proteins for correlative in-resin super-resolution and electron micro-scopy, Methods Cell Biol. 140 (2017) 49–67.

[108] J.P. Heller, D.A. Rusakov, A method to visualize the nanoscopic morphology of astrocytes in vitro and in situ, Methods Mol. Biol. 2019 (1938) 69–84.

[109] F. Herrmannsdorfer, B. Flottmann, S. Nanguneri, V. Venkataramani, H. Horstmann, T. Kuner, M. Heilemann, 3D d STORM imaging of fixed brain tissue, Methods Mol. Biol. 1538 (2017) 169–184.

[110] C.S. Smith, N. Joseph, B. Rieger, K.A. Lidke, Fast, single-molecule localization that achieves theoretically minimum uncertainty, Nat. Methods 7 (5) (2010) 373–375.

[111] R.E. Thompson, D.R. Larson, W.W. Webb, Precise nanometer localization analysis for individual fluorescent probes, Biophys. J. 82 (5) (2002) 2775–2783.

[112] R. Henriques, M. Lelek, E.F. Fornasiero, F. Valtorta, C. Zimmer, M.M. Mhlanga, QuickPALM: 3D real-time photoactivation nanoscopy image processing in ImageJ, Nat. Methods 7 (5) (2010) 339–340.

[113] M. Ovesny, P. Krizek, J. Borkovec, Z. Svindrych, G.M. Hagen, ThunderSTORM: a comprehensive ImageJ plug-in for PALM and STORM data analysis and super-resolution imaging, Bioinformatics 30 (16) (2014) 2389–2390.

[114] D.A. Rusakov, E. Harrison, M.G. Stewart, Synapses in hippocampus occupy only 1–2% of cell membranes and are spaced less than half-micron apart: a quantitative ultrastructural analysis with discussion of physiological implications, Neuropharmacology 37 (4–5) (1998) 513–521.

[115] A. Dani, B. Huang, J. Bergan, C. Dulac, X. Zhuang, Superresolution imaging of chemical synapses in the brain, Neuron 68 (5) (2010) 843–856.

[116] M. Igarashi, M. Nozumi, L.G. Wu, F. Cella Zanacchi, I. Katona, L. Barna, P. Xu, M. Zhang, F. Xue, E. Boyden, New observations in neuroscience using super-resolution microscopy, J. Neurosci. 38 (44) (2018) 9459–9467.

[117] J. Tonnesen, U.V. Nagerl, Superresolution imaging for neuroscience, Exp. Neurol. 242 (2013) 33–40.

[118] J. Tonnesen, V. Inavalli, U.V. Nagerl, Super-resolution imaging of the extracellular space in living brain tissue, Cell 172 (5) (2018) . 1108–1121 e15.

[119] J.M. Masch, H. Steffens, J. Fischer, J. Engelhardt, J. Hubrich, J. Keller-Findeisen, E. D'Este, N.T. Urban, S.G.N. Grant, S.J. Sahl, D. Kamin, S.W. Hell, Robust nano-scopy of a synaptic protein in living mice by organic-fluorophore labeling, PNAS 115 (34) (2018) E8047–E8056.

[120] T.L. Liu, S. Upadhyayula, D.E. Milkie, V. Singh, K. Wang, I.A. Swinburne, K.R. Mosaliganti, Z.M. Collins, T.W. Hiscock, J. Shea, A.Q. Kohrman, T.N. Medwig, D. Dambournet, R. Forster, B. Cunniff, Y. Ruan, H. Yashiro, S. Scholpp, E.M. Meyerowitz, D. Hockemeyer, D.G. Drubin, B.L. Martin, D.Q. Matus, M. Koyama, S.G. Megason, T. Kirchhausen, E. Betzig, Observing the cell in its native state: Imaging subcellular dynamics in multicellular organisms, Science 360 (6386) (2018).

[121] R. Turcotte, Y. Liang, M. Tanimoto, Q. Zhang, Z. Li, M. Koyama, E. Betzig, N. Ji, Dynamic super-resolution structured illumination imaging in the living brain, Proc. Nat. Acad. Sci. U. S. A. (2019).

[122] A. Minelli, P. Barbaresi, R.J. Reimer, R.H. Edwards, F. Conti, The glial glutamate transporter GLT-1 is localized both in the vicinity of and at distance from axon terminals in the rat cerebral cortex, Neuroscience 108 (1) (2001) 51–59.